• Original Paper •

Spatiotemporal Evaluation and Future Projection of Diurnal Temperature Range over the Tibetan Plateau in CMIP6 Models

Suguo ZHANG[1,4], Qin HU[*1,5], Xianhong MENG[2], Yaqiong LÜ[3], and Xianyu YANG[1]

[1]*School of Atmospheric Sciences/ Plateau Atmosphere and Environment Key Laboratory of Sichuan Province*,
Chengdu University of Information Technology, *Chengdu* 610225, *China*
[2]*Northwest Institute of Eco-Environment and Resources*, *Chinese Academy of Sciences*, *Lanzhou* 730000, *China*
[3]*Institute of Mountain Hazards and Environment*, *Chinese Academy of Sciences*, *Chengdu* 610041, *China*
[4]*School of Atmospheric Sciences*, *Sun Yat-sen University*, *Zhuhai* 519082, *China*
[5]*Earth System Modelling*, *School of Engineering and Design*, *Technical University of Munich*, *Munich* 85521, *Germany*

ABSTRACT

The diurnal temperature range (DTR) serves as a vital indicator reflecting both natural climate variability and anthropogenic climate change. This study investigates the historical and projected multitemporal DTR variations over the Tibetan Plateau. It assesses 23 climate models from phase 6 of the Coupled Model Intercomparison Project (CMIP6) using CN05.1 observational data as validation, evaluating their ability to simulate DTR over the Tibetan Plateau. Then, the evolution of DTR over the Tibetan Plateau under different shared socioeconomic pathway (SSP) scenarios for the near, middle, and long term of future projection are analyzed using 11 selected robustly performing models. Key findings reveal: (1) Among the models examined, BCC-CSM2-MR, EC-Earth3, EC-Earth3-CC, EC-Earth3-Veg, EC-Earth3-Veg-LR, FGOALS-g3, FIO-ESM-2-0, GFDL-ESM4, MPI-ESM1-2-HR, MPI- ESM1-2-LR, and INM-CM5-0 exhibit superior integrated simulation capability for capturing the spatiotemporal variability of DTR over the Tibetan Plateau. (2) Projection indicates a slightly increasing trend in DTR on the Tibetan Plateau in the SSP1-2.6 scenario, and decreasing trends in the SSP2-4.5, SSP3-7.0, and SPP5-8.5 scenarios. In certain areas, such as the southeastern edge of the Tibetan Plateau, western hinterland of the Tibetan Plateau, southern Kunlun, and the Qaidam basins, the changes in DTR are relatively large. (3) Notably, the warming rate of maximum temperature under SSP2-4.5, SSP3-7.0, and SPP5-8.5 is slower compared to that of minimum temperature, and it emerges as the primary contributor to the projected decrease in DTR over the Tibetan Plateau in the future.

Key words: Tibetan Plateau, CMIP6 models, diurnal temperature range, model assessment, historical period, future projection

Citation: Zhang, S. G., Q. Hu, X. H. Meng, Y. Q. Lu, and X. Y. Yang, 2024: Spatiotemporal evaluation and future projection of diurnal temperature range over the Tibetan Plateau in CMIP6 models. *Adv. Atmos. Sci.*, https://doi.org/10.1007/s00376-024-3346-0.

Article Highlights:

• Most CMIP6 models successfully capture the spatiotemporal variability of DTR over the Tibetan Plateau.
• Future projections indicate declining (slightly increasing) DTR trends under SSP2-4.5, SSP3-7.0, and SPP5-8.5 (SSP1-2.6).
• The rate of increase for T_{max} is slower than T_{min}, which primarily contributes to the reduction in DTR.

---

1. Introduction

The global climate has been experiencing notable changes attributable to nearly a century of global warming, and recent evidence suggests that the severity of climate change might be more significant than previously anticipated (IPCC, 2021). Although the mean surface temperature is often emphasized as a crucial variable in assessing climate change, many earth system processes are influenced by extreme temperature fluctuations, extending beyond changes in mean values. The diurnal temperature range (DTR), reflecting the distinction between daily maximum and minimum temperatures, serves as a comprehensive metric

---

* Corresponding author: Qin HU
  Email: hq@cuit.edu.cn

that combines information on temperature extremes and consistently responds to anthropogenic greenhouse gas emissions (Karl et al., 1993; New et al., 2000; Vose et al., 2005). Given that minimum temperature hinges on longwave radiation and maximum temperature on shortwave radiation (Wang and Dickinson, 2013), the DTR serves as an intuitive measure of severe weather intensity and rapid short-term climate changes. Additionally, long-term changes in DTR impact various facets, including urban ecology, agricultural production, and human health (Lobell, 2007; Ren and Zhou, 2014; Christidis et al., 2019). Consequently, DTR has been identified as a fundamental index of climate dynamics by the World Climate Research Program (WCRP) and serves as a valuable benchmark for assessing the ability of numerous climate models to evaluate local climate change within the context of global warming (Hansen et al., 1995; Braganza et al., 2004; Shahid et al., 2012).

Global mean temperatures have risen at a rate exceeding $0.1°C (10 \text{ yr})^{-1}$ since 1950 (IPCC, 2021). This rise in mean temperature has been accompanied by a less pronounced increase in maximum temperatures compared to minimum temperatures, consequently leading to a significant decrease in the DTR (Karl et al., 1991; Vose et al., 2005; Wang et al., 2012). Similarly, observations in China and its subregions also depict a decreasing trend in DTR (Wang et al., 2012; Ren and Zhou, 2014; Shen et al., 2014; You et al., 2016).

The Tibetan Plateau, as an influential climate-sensitive and vulnerable region, exerts significant impacts on both East Asia and the global climate, primarily due to the dynamic and thermal effects arising from its extensive topography and geomorphology (Wu et al., 2005; Zhou et al., 2009a; Yao et al., 2012). As an early and sensitive indicator of global warming, climate change on the Tibetan Plateau has garnered substantial attention (Su et al., 2013; You et al., 2017; Zhu and Yang, 2020; Cui et al., 2021; Hu et al., 2022). The DTR on the Tibetan Plateau has been decreasing at an approximate rate of $0.2°C (10 \text{ yr})^{-1}$ since the 1960s, with areas experiencing the most significant DTR reduction, like the southern fringe of the Himalayas, corresponding to regions with the most notable warming (Duan and Wu, 2006; You et al., 2016). However, capturing changes in DTR has posed challenges for climate models (Stone and Weaver, 2003). Factors such as cloud cover, soil moisture, and precipitation variability play significant roles in DTR dynamics (Karl et al., 1993; Wild et al., 2005; Zhou et al., 2009b; Wang et al., 2014). Previous models, such as those that participated in phases 3 and 5 of the Coupled Model Intercomparison Project (CMIP3 and CMIP5, respectively), simulated global DTR values lower than those observed since 1950 (Lewis and Karoly, 2013). Although the CMIP5 models generally reproduced the spatial and temporal evolution of DTR on the Tibetan Plateau, they underestimated the magnitude of the changes (You et al., 2017).

Presently, the WCRP is conducting phase 6 of the Coupled Model Intercomparison Project (CMIP6), involving global climate modeling teams from various research institutions in numerical experiments with new models. These models are being provided to scientists to study global and regional climate change, along with its impacts and responses. Wang and Clow (2020) found that, at a worldwide scale, CMIP6-simulated DTR values were lower than observed values, with some models overestimating DTR at high latitudes in the Northern Hemisphere. Wang et al. (2024) found that CMIP6 models could reflect the decreasing trend of DTR during 1901–2014 globally. Liu et al. (2022) found the winter DTR exhibits a continuous declining trend in the historical and the future SSP2-4.5 scenario in East Asia. Despite CMIP6 models having higher resolution and relatively better simulation of extreme temperatures than CMIP5 models (Di Luca et al., 2020), their ability to simulate DTR at a global scale has remained relatively static. CMIP6 models outperform CMIP5 models only during the period of rapid DTR decrease from 1951 to 1980 (Wang and Clow, 2020). At the regional scale, evaluations of historical simulations indicate that CMIP6 models generally reproduce the spatial and temporal distribution characteristics of DTR in large regions, encompassing East Asia, China, and even smaller areas like the North China Plain and the southern Himalayan slopes (Hamal et al., 2021; Liu et al., 2022; Wang et al., 2022a, b).

However, the spatiotemporal simulation capability of the CMIP6 models for DTR on the Tibetan Plateau has yet to undergo a comprehensive evaluation and necessitates further investigation. Additionally, examining the future changes in DTR on the Tibetan Plateau under various Shared Socioeconomic Pathway (SSP) scenarios for the 21st century holds substantial significance and requires in-depth analysis. The goal of this study is to address these knowledge gaps and, in doing so, provide insights into integrated disaster mitigation and prevention strategies on the Tibetan Plateau.

2.   Region, data and methods

2.1.   *Study region*

The Tibetan Plateau, mainly situated in the southwestern part of China, spans the geographical coordinates of 25°–40°N and 70°–105°E. Recognized as Earth's "third pole", it encompasses an area of approximately 2.5 million square kilometers and boasts an average altitude surpassing 4500 m. Endowed with distinctive ecological features, it has developed a unique ecological pattern due to its unique geographical and climatic settings. The specific study area featured in this paper is depicted in Fig. 1.

2.2.   *Data*

2.2.1.   *Observed data*

The observational data utilized in this study are from the CN05.1 dataset, extending to the latest available period provided by the National Climate Center of China. These observations span from 1961 to 2022 and are compiled from an extensive collection of values sourced from over 2400
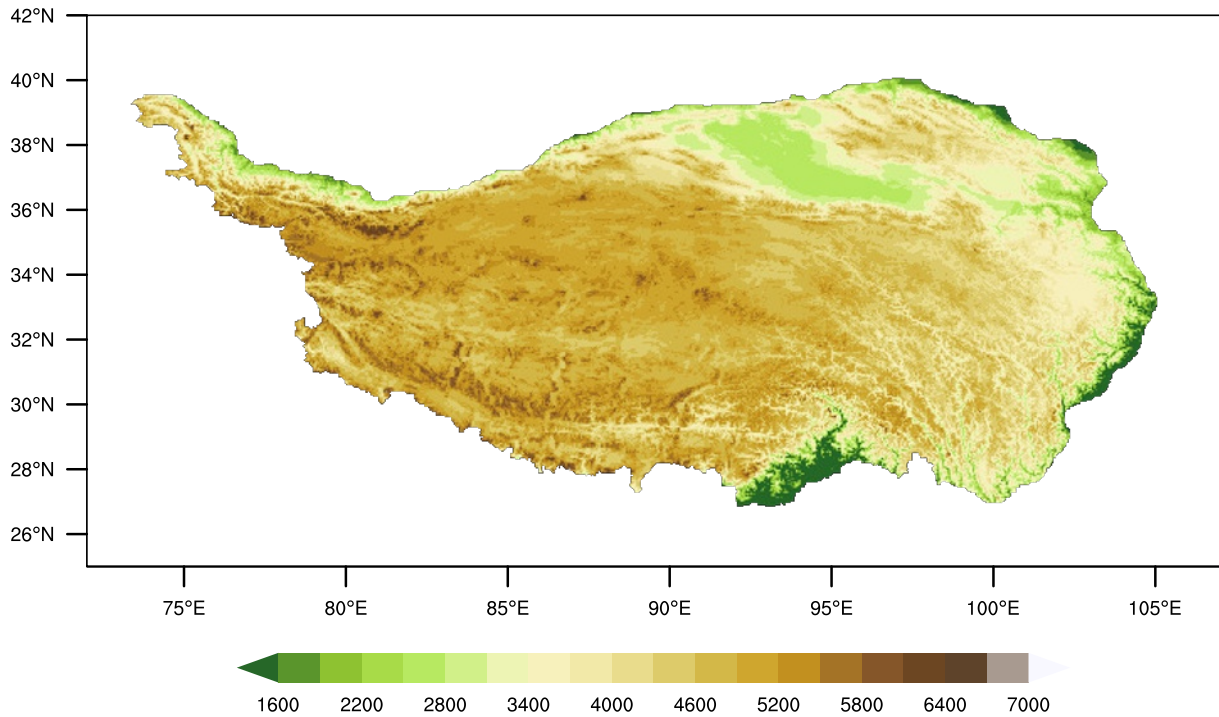
Fig. 1. Topographic map of the Tibetan Plateau (units: m).

major domestic ground-based meteorological stations. The dataset provides information at a resolution of $0.25° × 0.25°$ based on real-time monitoring records and was derived through the "anomaly approach" interpolation method; plus, it also offers $0.5° × 0.5°$ and $1.0° × 1.0°$ resolution data (Wu and Gao, 2013). It encompasses several primary variables: mean temperature, maximum temperature, minimum temperature, precipitation, surface evaporation, wind speed, and relative humidity. For this study, the monthly maximum, minimum, and mean temperature records of the $0.5° × 0.5°$ resolution dataset were selected.

2.2.2. *Simulation data*

For the assessment, this study employed the monthly historical simulation results obtained from 23 CMIP6 models, including all models that have SSP scenario data. To ensure consistent weighting of each model in the calculation, only the data with the r1i1p1f1 variant label were selected. The historical assessment period spans from 1995 to 2014, while the future projection period extends from 2022 to 2100. To analyze potential changes in DTR across different stages in the future, we divided the projection period into three subperiods: 2022–40 (near-term of the 21st century), 2040–60 (midterm), and 2080–2100 (long-term), following the CMIP-divided analysis periods (Eyring et al., 2016).

The study uses 23 models from the Tier-1 core experiment of the Scenario Model Comparison Program, covering four SSPs: SSP1-2.6, SSP2-4.5, SSP3-7.0, and SSP5-8.5. These scenarios project climate change over the Tibetan Plateau, ranging from low- to high-emission scenarios, aiming to contribute to reducing the future disaster risks associ-

ated with DTR. Additionally, the data are available for download, and further details can be accessed by searching at https://esgf-node.llnl.gov/projects/cmip6/. Note that some models do not provide outputs for SSP1-2.6 and SSP3-7.0, as indicated in Table 1.

2.3. *Methods*

In this paper, the DTR values over the Tibetan Plateau were calculated utilizing the CN05.1 observation data (Wu and Gao, 2013) alongside historical simulations from the 23 CMIP6 models. Consequently, the ability of these 23 models to reproduce the DTR over the Tibetan Plateau was evaluated with respect to the observed data, enabling the identification of models exhibiting superior simulation performance. These selected models were then used to project future DTR changes across the Tibetan Plateau.

For model evaluation, a bilinear interpolation method was employed to interpolate the simulated model data uniformly and observed data onto a $0.5° × 0.5°$ resolution. This facilitated a comparison between the 23 model datasets and the measured data while exploring the comprehensive simulation effects of the models.

To evaluate the simulation ability of each model for the DTR of the Tibetan Plateau, we utilized various metrics such as the correlation coefficient, root-mean-square error, and the ratio of standard deviation between model data and observational data over time. These metrics are graphically represented on a Taylor diagram to visualize and analyze the simulation capacity of the 23 models concerning the temporal and spatial variation of the DTR over the Tibetan Plateau during the historical period:

Table 1. Basic information on the 23 CMIP6 models employed in this study.

Model name	Nation and institute	Horizontal Resolution (lon×lat)	SSP1-2.6	SSP2-4.5	SSP3-7.0	SSP5-8.5
ACCESS-CM2	Australia, CSIRO-ACCESS	192 × 144	√	√	√	√
ACCESS-ESM1-5	Australia, CSIRO-ACCESS	192 × 145	√	√	√	√
AWI-CM-1-1-MR	Germany, AWI	384 × 192	√	√	√	√
BCC-CSM2-MR	China, BCC	320 × 160	√	√	√	√
CanESM5	Canada, CCCma	128 × 64	√	√	√	√
CAS-ESM2.0	China, IAP-CAS	256 × 128	√	√	√	√
CIESM	China, THU	288 × 192	√	√	×	√
CMCC-ESM2	Italy, CMCC	288 × 192	√	√	√	√
EC-Earth3	Multinational, AEMET etc.	512 × 256	√	√	√	√
EC-Earth3-CC	Multinational, AEMET etc.	512 × 256	×	√	×	√
EC-Earth3-Veg	Multinational, AEMET etc.	512 × 256	√	√	√	√
EC-Earth3-Veg-LR	Multinational, AEMET etc.	320 × 160	√	√	√	√
FGOALS-g3	China, IAP-CAS	180 × 80	√	√	√	√
FIO-ESM-2-0	China, FIO	288 × 192	√	√	×	√
GFDL-ESM4	USA, GFDL	288 × 180	√	√	√	√
INM-CM4-8	Russia, INM	180 × 120	√	√	√	√
INM-CM5-0	Russia, INM	180 × 120	√	√	√	√
IPSL-CM6A-LR	France, IPSL	144 × 143	√	√	√	√
MIROC6	Japan, MIROC	256 × 128	√	√	√	√
MPI-ESM1-2-HR	Japan, MRI	320 × 160	√	√	√	√
MPI-ESM1-2-LR	Japan, MRI	192 × 96	√	√	√	√
MRI-ESM2.0	Japan, MRI	320 × 160	√	√	√	√
NESM3	China, NUIST	192 × 96	√	√	×	√

$$\text{RMSE} = \sqrt{\frac{1}{N}\sum_{i=1}^{n}(X_{o,i} - X_{m,i})^2}, \tag{1}$$

$$\sigma_m = \sqrt{\frac{\sum_{i=1}^{n}(X_{m,i} - \overline{X}_m)^2}{n-1}}, \tag{2}$$

$$\sigma_o = \sqrt{\frac{\sum_{i=1}^{n}(X_{o,i} - \overline{X}_o)^2}{n-1}}, \tag{3}$$

$$\text{bias} = \frac{(\overline{X}_m - \overline{X}_o)}{\overline{X}_o}, \tag{4}$$

$$R = \frac{\sum_{i=1}^{n}(X_{o,i} - \overline{X}_o)(X_{m,i} - \overline{X}_m)}{\sqrt{\sum_{i=1}^{n}(X_{o,i} - \overline{X}_o)^2}\sqrt{\sum_{i=1}^{n}(X_{m,i} - \overline{X}_m)^2}}, \tag{5}$$

where $X_{o,i}$ and $X_{m,i}$ stand for the DTR values of the observation and simulation, and $\overline{X}_o$ and $\overline{X}_m$ denote the mean values of the observed and simulated DTR, respectively; RMSE refers to the root-mean-square error; σ_o and σ_m represent the standard deviations of the observation and the model,

respectively; and R signifies the correlation coefficient between the observation and the model.

In order to minimize the influence of individual CMIP6 model errors on the projected results, the multimodel median was used:

$$X_{\text{median}} = \begin{cases} x_{\frac{n+1}{2}}, & \text{if } n \text{ is odd} \\ \frac{1}{2}\left(x_{\frac{n}{2}} + x_{\frac{n}{2}+1}\right), & \text{if } n \text{ iseven} \end{cases}, \tag{6}$$

where n represents the number of models involved in the calculation. Each grid cell participates individually in the calculation of the multimodel median for each monthly time step.

3.   Results

3.1.   *Evaluation of DTR simulation*

3.1.1.   *Climatological average state*

The climatological spatial distribution of the DTR over the Tibetan Plateau from 1995 to 2014 is represented in Fig. 2, showcasing comparisons between the CN05.1 observations and the CMIP6 models. The observed DTR reveals specific patterns: Areas in the eastern and western hinterlands, as well as the Qaidam Basin, show larger zones with DTR values exceeding 14°C. In contrast, the eastern and southeastern mountainous edge regions of the Tibetan Plateau, and the eastern Pamir Plateau, exhibit relatively minor DTR values, ranging between 6°C and 8°C.
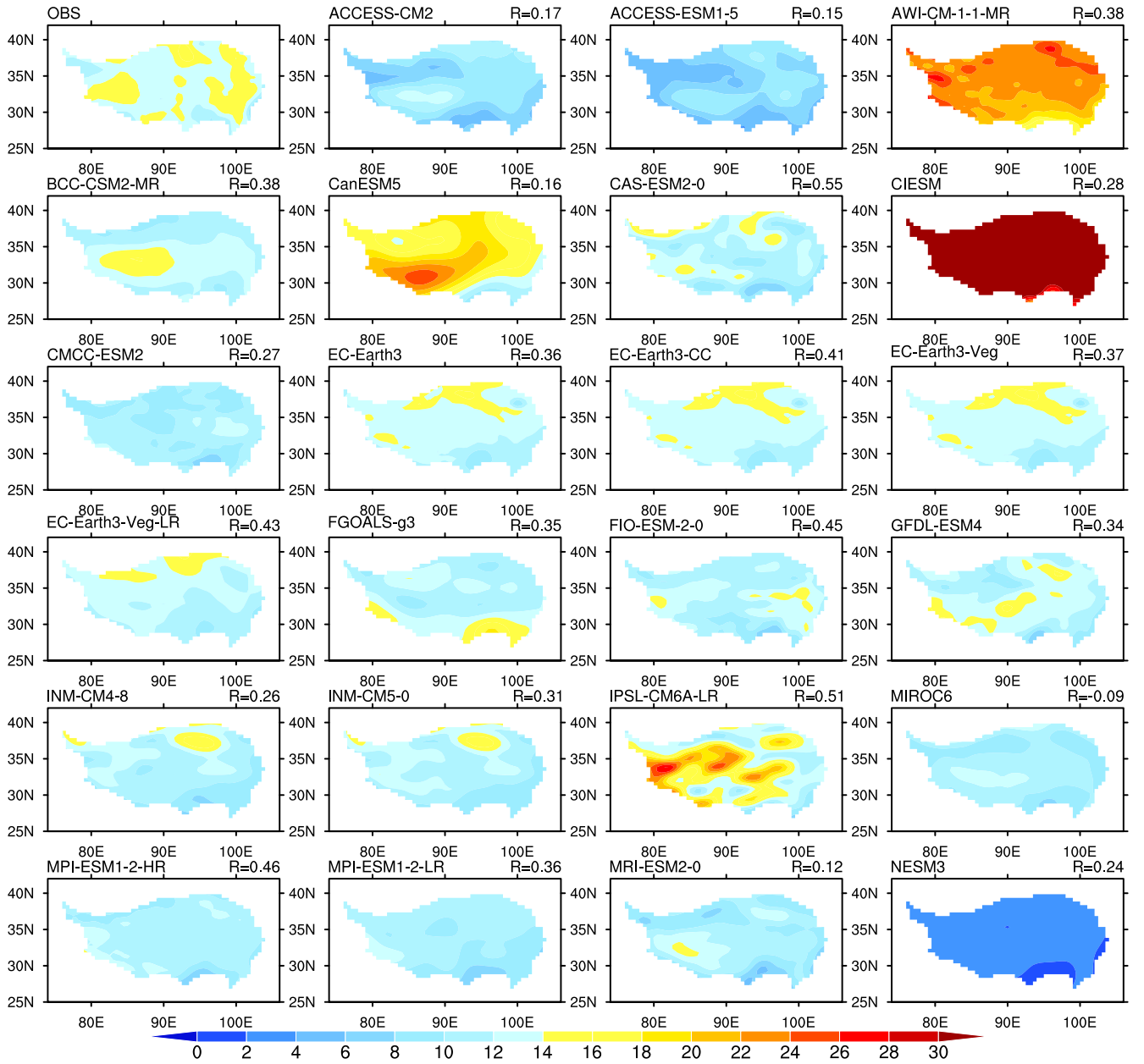
Fig. 2. Spatial distribution of the climatological mean state of DTR simulated by CN05.1 observations and 23 CMIP6 models from 1995 to 2014 (units: °C). *R* represents the spatial correlation coefficient between the model and the observation.

The assessment of the CMIP6 model simulations demonstrates varied degrees of overestimation or underestimation of the DTR across different subregions of the Tibetan Plateau, particularly highlighted in the case of the CIESM and NESM3 models. The former exhibits a notable degree of overestimation, indicating a minimum DTR value of up to 25°C and a maximum value of 60.4°C. In contrast, the latter model significantly underestimates the DTR, with a maximum value of only 4.5°C.

Comparing these findings with observational data, some models, such as EC-Earth3, EC-Earth3-CC, and EC-Earth3-Veg, simulate the distribution better in both low and high-value regions, approaching values observed in the data. On the other hand, six models—BCC-CSM2-MR,

CAS-ESM2-0, CMCC-ESM2, EC-Earth3-Veg-LR, MPI-ESM1-2-HR, and MPI-ESM1-2-LR—better simulate low-value areas but are less accurate in high-value areas. Conversely, INM-CM4-8 and INM-CM5-0 depict good simulations for high-value areas but perform poorly for low-value areas. The models with relatively good spatial correlation coefficients are CAS-ESM2-0, IPSL-CM6A-LR, EC-Earth3-Veg-LR, MPI-ESM1-2-HR, FIO-ESM-2-0, and EC-Earth3-CC, for which the correlation coefficients exceed 0.4. In summary, the DTR simulations from various models for different subregions of the Tibetan Plateau display varying degrees of overestimation or underestimation, but some models can capture the spatial distribution characteristics of the DTR across the Tibetan Plateau.

3.1.2. *Inter-monthly variation*

In order to evaluate each model's ability to reproduce the monthly variation of DTR, the climatological annual cycle of area-averaged DTR over the Tibetan Plateau is depicted in Fig. 3, showcasing observations and the results from 23 CMIP6 models. According to the observed data, the highest DTR value occurs in December, at 15.4°C, while the lowest value is recorded in July, at around 11°C. Comparing the observed spatial distribution of DTR in Fig. 2 and prior research, it is apparent that the DTR over the Tibetan Plateau exceeds that of eastern China during the same period, displaying a significant diurnal variation and a pronounced sensitivity to changes between July to September and December to February.

Upon analyzing the CMIP6 model simulations, several models—namely, EC-Earth3-CC, MPI-ESM1-2-HR, EC-Earth3-Veg, MPI-ESM1-2-LR, EC-Earth3, GFDL-ESM4, IPSL-CM6A-LR, CAS-ESM2-0, Can ESM5, and EC-Earth3-Veg-LR—demonstrate commendable accuracy in replicating the monthly variational trend of DTR, and their temporal correlation coefficients with observations surpass 0.93. These models closely align with the observed peak and trough occurrence times. However, MPI-ESM1-2-HR and MPI-ESM1-2-LR slightly underpredict the peak compared to observations, while EC-Earth3-CC and EC-Earth3-

Veg provide a closer match. Conversely, MIROC6 shows a trend opposite to the observed data, whereas CIESM and NESM exhibit significant deviation in simulating maximum and minimum values, indicating the poorest performance among the models. The remaining models display various deviation levels in peak or trough timings, and some reveal multiple peaks or troughs, suggesting moderate simulation capabilities. Therefore, further quantitative assessments are necessary to enhance their accuracy and reliability.

3.1.3. *Quantitative evaluation of CMIP6 simulation ability*

The selection of models demonstrating strong simulation capabilities for the spatiotemporal variation of DTR will be a focus in this part of the study for future projections of the DTR trend over the Tibetan Plateau. To appraise the capacity of the 23 CMIP6 models to simulate DTR variation over the Tibetan Plateau, we assess the temporal correlation coefficients, standard deviation ratios, and RMSE between the simulated and observed DTR data after normalization from 1995 to 2014. These results are visualized in a Taylor diagram, as depicted in Fig. 4. In this diagram, the horizontal and vertical axes represent normalized standard deviations, indicating the ratio of model standard deviation to that of observations. The radial lines illustrate the correlation coefficients, signifying the correlation between observed and model data. Addi-
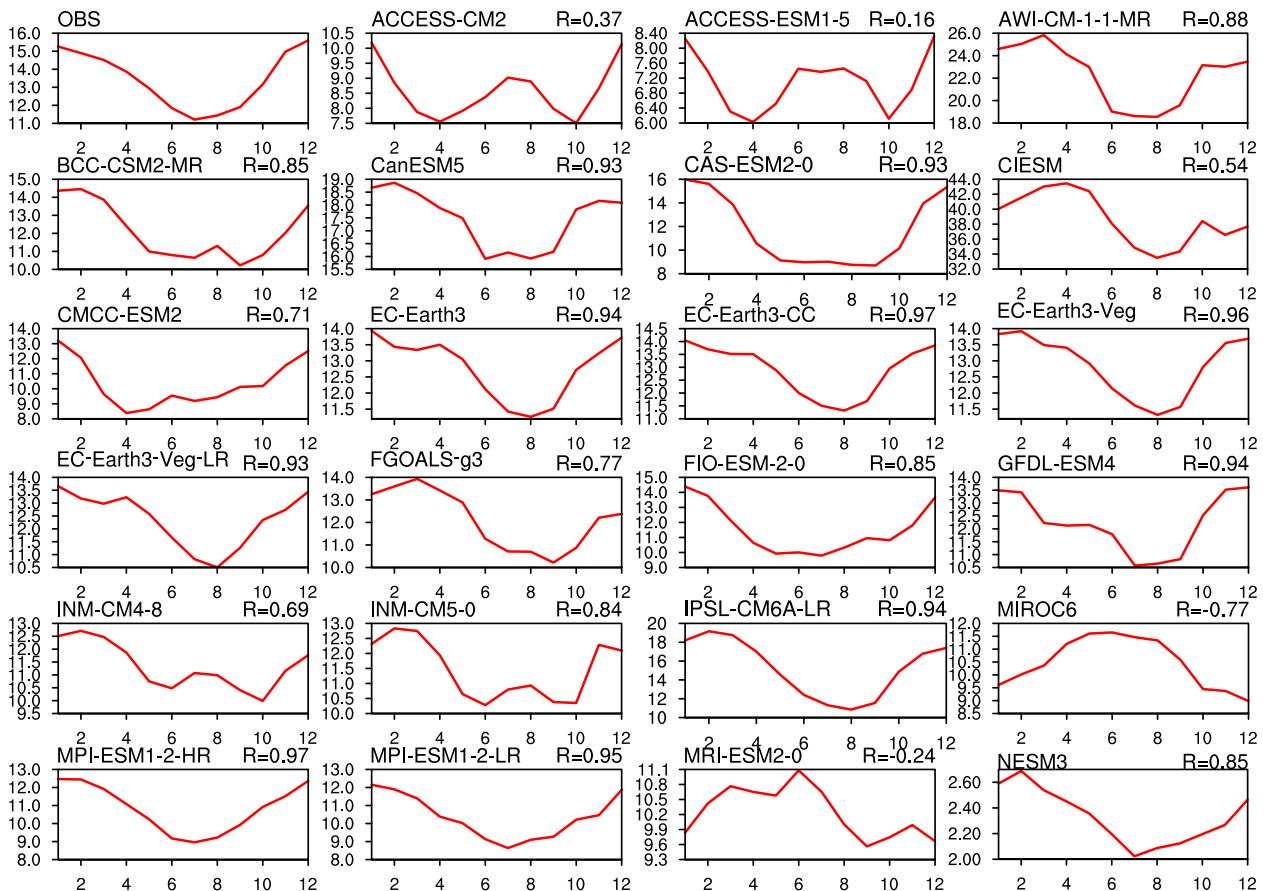

Fig. 3. Monthly area-averaged DTR during 1995–2014 over the Tibetan Plateau simulated by CN05.1 observations and 23 CMIP6 models (units: °C). *R* denotes the temporal correlation coefficient between the model and the observation.

tionally, the arcs from the point labelled REF at the origin illustrate the RMSE, with values spaced at intervals of 0.25, 0.5, 0.75, and 1. The closer the model results are to a normalized standard deviation of 1, correlation coefficient of 1, and RMSE of 0, the better the agreement between the model simulations and observed data.

Figure 4 indicates that the correlation coefficients of all models successfully passed the significance test at the 95% confidence level. The BCC-CSM2-MR, EC-Earth3, EC-Earth3-CC, EC-Earth3-Veg, EC-Earth3-Veg-LR, FGOALS-g3, FIO-ESM-2-0, GFDL-ESM4, MPI -ESM1-2-HR, MPI-ESM1-2-LR, INM-CM5-0 and CanESM5 models show robust correlation coefficients of more than 0.65, which range from 0.67–0.87, indicating a high level of agreement between their simulations and observed DTR variations. The standard deviation ratios between the simulated and observed DTR for BCC-CSM2-MR, CMCC-ESM2, and FIO-ESM-2-0 are close to 1, at 0.98, 0.99, and 1.01, respectively, suggesting that the interannual DTR variation in these models closely resembles that of the observations, indicating a more accurate representation. Furthermore, compared with the other models, BCC-CSM2-MR, EC-Earth3, EC-Earth3-CC, EC-Earth3-Veg, EC-Earth3-Veg-LR, FGOALS-g3, FIO-ESM-2-0, GFDL-ESM4, MPI-ESM1-2-HR, MPI- ESM1-2-LR, and INM-CM5-0 have relatively

small RMSEs of less than 0.75, which suggests these models display less deviation from the observed data, strengthening their robust performance in simulating DTR variation. However, CIESM and NESM3 perform poorly in simulating the spatial and temporal evolution of DTR on the Tibetan Plateau. Excluding CIESM and NESM3, the simulations from the other models demonstrate smaller biases compared to the observed results. Moreover, the mean DTRs of EC-Earth3-CC, EC-Earth3-Veg, EC-Earth3-Veg, EC-Earth3, FGOALS-g3, IPSL-CM6A-LR, and GFDL-ESM4 are very close to the observations. The majority of CMIP6 models exhibit plausible results in simulating DTR variation over the Tibetan Plateau. Several models show general agreement with observations regarding the mean, bias, correlation, standard deviation, and RMSE.

Consequently, models with a temporal correlation coefficient greater than 0.65, spatial correlation coefficient greater than 0.3, RMSE less than 0.75, and standard deviation ratio between 0.65 and 1 were selected as models with relatively good simulation performance for further projection. These selected CMIP6 models are BCC-CSM2-MR, EC-Earth3, EC-Earth3-CC, EC-Earth3-Veg, EC-Earth3-Veg-LR, FGOALS-g3, FIO-ESM-2-0, GFDL-ESM4, MPI-ESM1-2-HR, MPI-ESM1-2-LR, and INM-CM5-0.
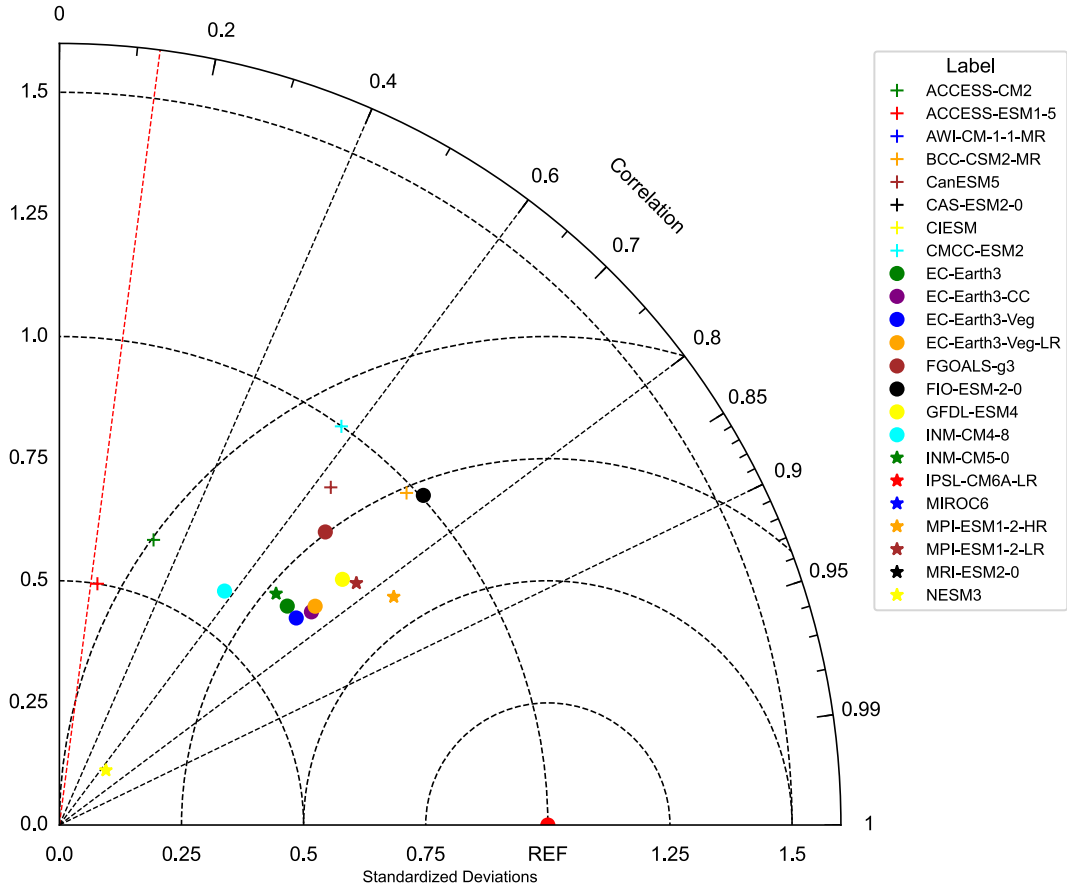

Fig. 4. Taylor diagram of DTR simulated by CMIP6 models from 1995 to 2014 (the red dotted line indicates that the correlation coefficient passes the significance test with confidence of 95%).

3.2. *Future projection of DTR over the Tibetan Plateau based on selected CMIP6 models*

Based on the previous analysis, 11 models (BCC-CSM2-MR, EC-Earth3, EC-Earth3-CC, EC-Earth3-Veg, EC-Earth3-Veg-LR, FGOALS-g3, FIO-ESM-2-0, GFDL-ESM4, MPI-ESM1-2-HR, MPI-ESM1-2-LR, and INM-CM5-0) were selected for their relatively greater ability to simulate the spatial and temporal variations of DTR on the Tibetan Plateau from 1995 to 2014. These chosen models are employed to investigate the future trends of DTR on the Tibetan Plateau throughout the 21st century. To better understand the potential changes in DTR at various stages in the future, the entire future projection period was segmented into three subperiods: 2022–40, 2040–60, and 2080–2100, categorized as the near-term, mid-term, and long-term of the 21st century, respectively, following the periods classified by CMIP analysis (Eyring et al., 2016).

3.2.1. *Temporal variation*

The annual average time series of the multimodel median DTR from the 11 selected CMIP6 models on the Tibetan Plateau under different scenarios is depicted in Fig. 5. The results demonstrate a decline in the regional average DTR across the SSP2-4.5, SSP3-7.0, SSP5-8.5 scenarios, but a less pronounced rate of increase under the SSP1-2.6 scenario. Analyzing the entire period from 2022 to 2100, the trend of DTR under the SSP1-2.6 scenario is upward, with a rate of $0.018°C (10 yr)^{-1}$, resulting in an approximate increase of $0.18°C$ from 2022 to the end of the century. In contrast, under the other three scenarios, the DTR experiences a general downward trend. The decline is less significant under the SSP2-4.5 scenario, with a trend of $-0.011°C (10 yr)^{-1}$, while the declines are more pronounced

under the SSP3-7.0 and SSP5-8.5 scenarios, at $-0.024°C$ and $-0.051°C (10 yr)^{-1}$, respectively.

However, during the subperiods, the trend varies slightly. In the near-term, unlike the entire period, there is a slight downward trend observed in DTR under the SSP1-2.6 scenario. Under the SSP2-4.5 and SSP3-7.0 scenarios, the declines are greater than that of the entire period. Under the SSP2-4.5 scenario, the DTR drops to $11.83°C$ in 2040, indicating an overall decrease of approximately $0.1°C$ from 2022 to 2040. Similar declining trends are observed under the SSP5-8.5 scenario, with declines of $0.1°C$. In the mid-term, the DTR under the SSP1-2.6 and SSP3-7.0 scenarios displays a slight upward trend. In contrast, SSP2-4.5 and SSP5-8.5 show similar declining trends in the near-term. Looking ahead to the long-term subperiod, the SSP1-2.6 scenario indicates an increase of $0.1°C$ compared to the near-term. However, under the other three scenarios, there is a notable reduction in DTR, becoming more prominent as radiative forcing increases. The DTR decreases by $0.13°C$, $0.25°C$, and $0.39°C$ under the SSP2-4.5, SSP3-7.0, and SSP5-8.5 scenarios, respectively. The most substantial decline in DTR is observed under the SSP5-8.5 scenario.

3.2.2. *Spatial distribution*

The spatial distribution variations in the DTR on the Tibetan Plateau under different SSP scenarios and policy measures is investigated in this section. Figure 6 illustrates the projected results of the multimodel median during the near, mid, and long term for different scenarios. The maximum DTR values are consistently concentrated in the Qaidam Basin and the Gangdise–Himalayan Mountains across all scenarios. In contrast, the minimum multimodel median DTR value is observed in the southeastern part of the Tibetan
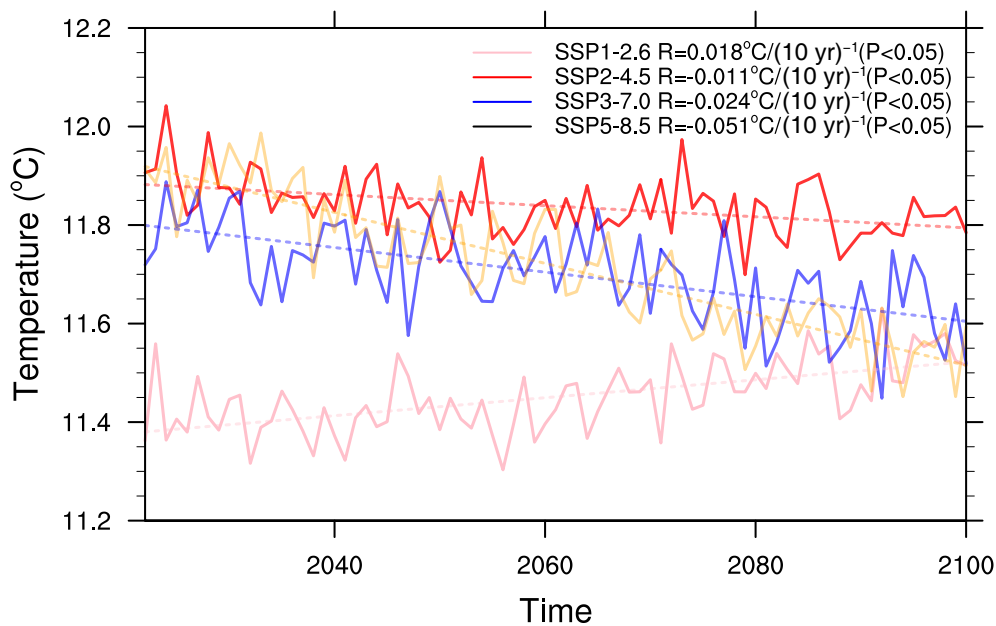

Fig. 5. Annual average time series of the multimodel median DTR over the Tibetan Plateau under four SSP scenarios in 2022–2100, in which the pink, red, blue, and yellow lines represent the SSP1-2.6, SSP2-4.5, SSP3-7.0, and SSP5-8.5 scenarios, respectively.
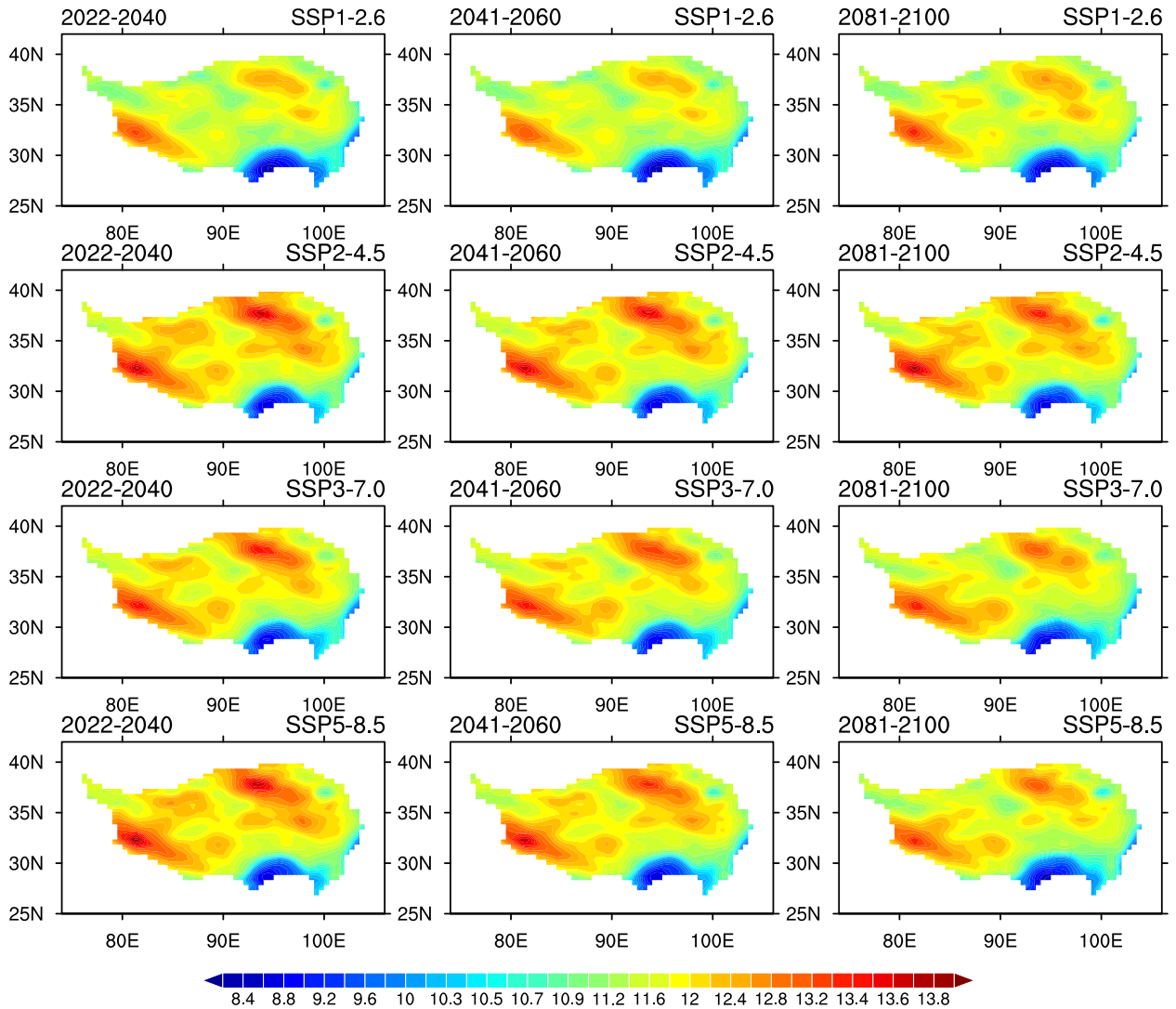
Fig. 6. Spatial distribution of the multimodel median DTR over the Tibetan Plateau in 2022–40, 2041–60, and 2081–2100 under different SSP scenarios (units: °C).

Plateau—specifically, in the Lhasa–Nyingchi region. The distribution and values of these extremities remain relatively stable over the years. Comparing this distribution to the climatology of DTR from 1995 to 2014, it can be seen that the maximum values have decreased by approximately 1°C–2°C, and their distribution range has expanded, particularly in the Gangdise–Himalayan Mountains. The distribution area of the large values has expanded southward, while the minimum values remain unchanged compared to the 1995–2014 period.

Using the projected results, we further analyze the spatial distribution of climatological changes in the multimodel median DTR over the three subperiods compared to the historical period of 1995–2014, as shown in Fig. 7. In each subperiod, the DTR undergoes relatively different changes under different SSP scenarios compared to the historical reference period. Positive values are evident across nearly all regions under the SSP1-2.6 and SSP3-7.0 scenarios throughout all subperiods, except for the southeastern edge of the Tibetan

Plateau, and in most regions under the SSP5-8.5 scenario in the long term. Conversely, negative values are notable under the SSP2-4.5 scenario, and under SSP5-8.5 in the near-term and mid-term periods.

From the near- to long-term period, there is a slight increase in the median DTR distribution under the SSP1-2.6 scenario. The most notable increase occurs at the southeastern edge of the Tibetan Plateau and in the western hinterlands. However, under the SSP2-4.5, SSP3-7.0, and SSP5-8.5 scenarios, the DTR exhibits decreases in various areas from the near- to long-term period, especially under the SSP5-8.5 scenario. These changes become more pronounced in magnitude over the years. In the same subperiods, as the radiative forcing of the SSP scenarios increases, the area experiencing warming expands under SSP2-4.5 compared to SSP1-2.6. However, this trend reverses under SSP3-7.0 and SSP5-8.5, where the area of warming decreases compared to SSP2-4.5, particularly in the long term.

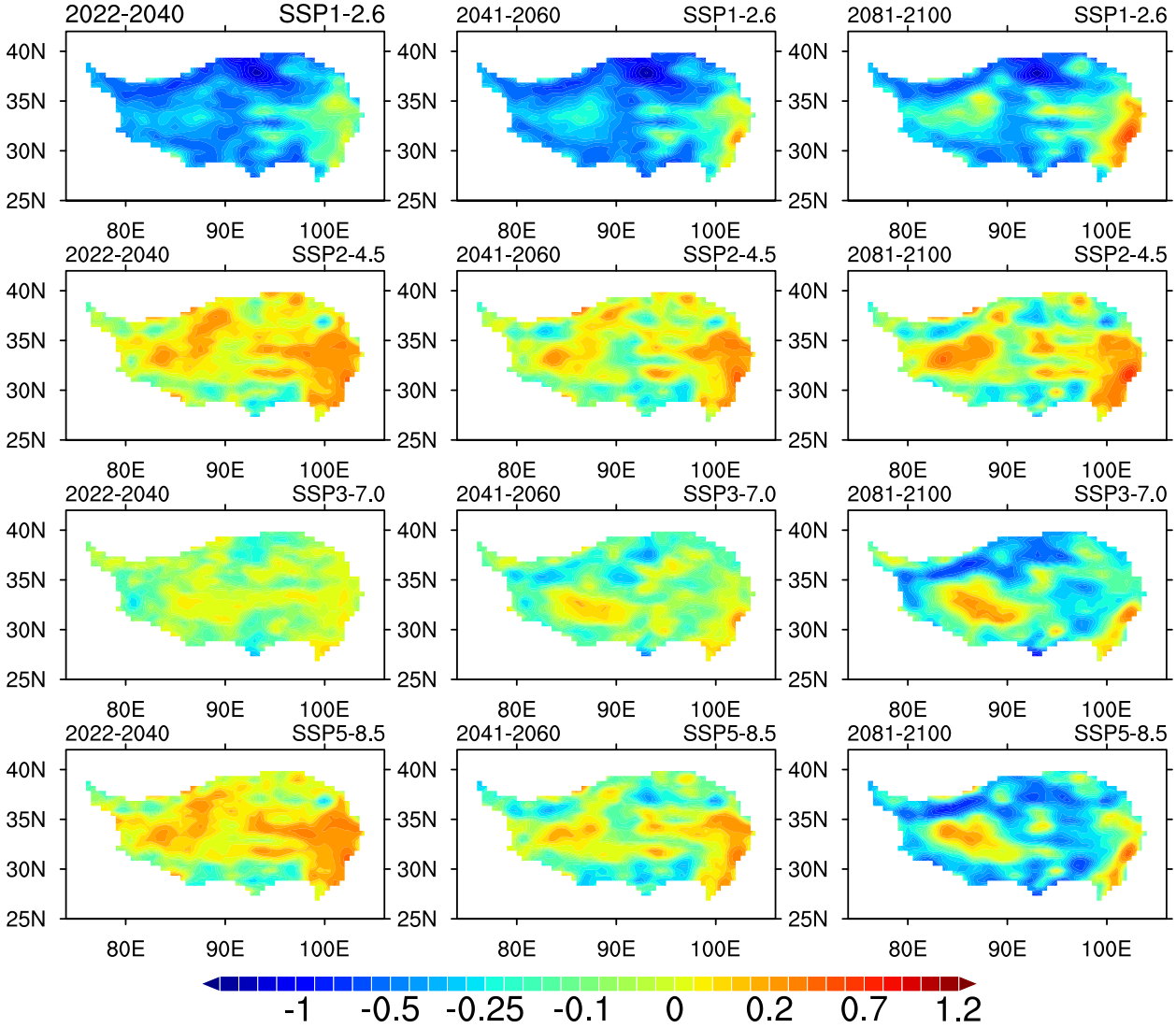Under the scenario of low radiative forcing and sustain-

Fig. 7. Spatial distribution of climatological changes in the multimodel median DTR over the Tibetan Plateau under different scenarios for 2022–40, 2041–60, and 2081–2100 compared to the historical period of 1995–2014 (units: °C).

able development, a modest increase in the DTR over the southeastern Tibetan Plateau is projected for the late 21st century. Conversely, in scenarios following conventional and high radiative forcing development pathways, the overall projection indicates a decrease in the DTR across the Tibetan Plateau by the late 21st century.

3.2.3. *Inhomogeneity of DTR variation*

To examine the direct reasons behind the variation in DTR across the various scenarios during the three subperiods, Fig. 8 depicts the annual average time series of the multimodel median DTR, T_{min} (minimum temperature), and T_{max} (maximum temperature) from 2022 to 2100 under four different scenarios. Under the SSP1-2.6, SSP2-4.5, SSP3-7.0, and SSP5-8.5 scenario, the changes in DTR are 0.018°C, −0.011°C, −0.024°C, and −0.051°C (10 yr)$^{-1}$, respectively.

Under the SSP1-2.6 scenario, there is a minimal rise in both T_{min} and T_{max}, with T_{max} experiencing a relatively larger increase than T_{min}, showing a warming trend rate 1.21 times that of T_{min}. As a result, there is a slight overall increase in DTR by the end of the century. Conversely, under the SSP2-4.5, SSP3-7.0, and SSP5-8.5 scenarios, T_{max} and T_{min} exhibit notable increases, but T_{min} experiences a more substantial rise than T_{max} in all three scenarios.

Specifically, under the SSP2-4.5 scenario, the warming trend rate of T_{min} is 1.06 times that of T_{max}. Under the SSP3-7.0 scenario, T_{min} warms at a trend rate 1.09 times that of T_{max}, and under the SSP5-8.5 scenario the warming trend rate of T_{min} is 1.1 times that of T_{max}. This variance in the warming trend rates between T_{min} and T_{max} leads to a decrease in DTR over the Tibetan Plateau by the end of the 21st century under these scenarios. In essence, the differing warming trend rates of T_{max} and T_{min} across the different scenarios, where T_{min} warms at a faster pace than T_{max}, contribute to varying levels of reduction in DTR on the Tibetan Plateau.
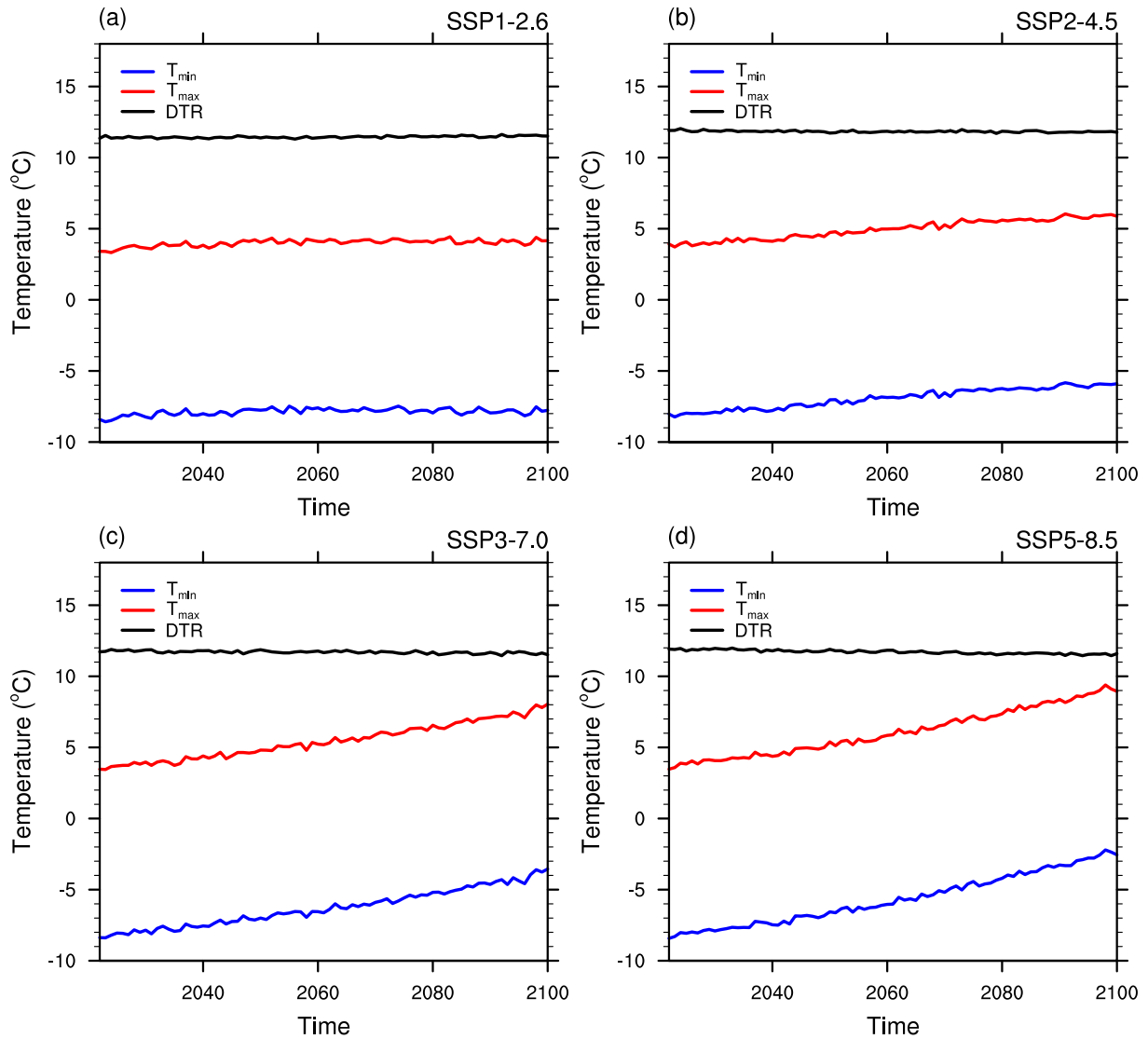
Fig. 8. Annual time series of the multimodel median DTR, T_{min}, and T_{max} under the (a) SSP1-2.6, (b) SSP2-4.5, (c) SSP3-7.0, and (d) SSP5-8.5 scenario for the period 2022–2100.

3.2.4. *Uncertainty among the models*

Uncertainty in model simulations can be categorized into internal variability, model uncertainty, and scenario uncertainty (Hawkins and Sutton, 2011). In addition, the uncertainty of the study results also stems from two factors: (1) The data utilized in this study consist of the maximum and minimum monthly temperature data. Given the relatively large time intervals considered in our research, the outcomes are expected to resemble those obtained using daily-scale data, thus minimizing potential errors. (2) The projections for DTR on the Tibetan Plateau for the 21st century involved selecting CMIP6 models with robust simulation performance. Human judgment errors may exist despite our statistically based selection process.

The projection results are based on the multimodel median of 11 selected CMIP6 models, and exploring the differences among models contributes to understanding the uncertainty of the future projection. The ranges of projected

DTR by each selected CMIP6 model under the four scenarios across near-, mid- and long-term periods are represented in Fig. 9. The differences between the minimum and maximum DTR projections among these models are within 2.5°, and the multimodel ensemble (MME) values are lower than the multimodel median values. However, the differences are not remarkable, ranging from approximately 0.15° to 0.42°. From the minimum and maximum projected DTR values, as well as the 25th and 75th percentiles values, it can be observed that there are models with exceptionally low results. In the long-term period, from the SSP1-2.6 to the SSP5-8.5 scenarios, the decreasing trend in DTR is evident.

The utilization of the multimodel median in projection likely mitigated model-induced errors. Moreover, compared to the MME, the influence of errors induced by a minority of models with cold bias is diminished. While acknowledging the uncertainties within our study, we maintain that the conclusion about the general declining trend of the DTR over the Tibetan Plateau under the SSP2-4.5, SSP3-7.0, and
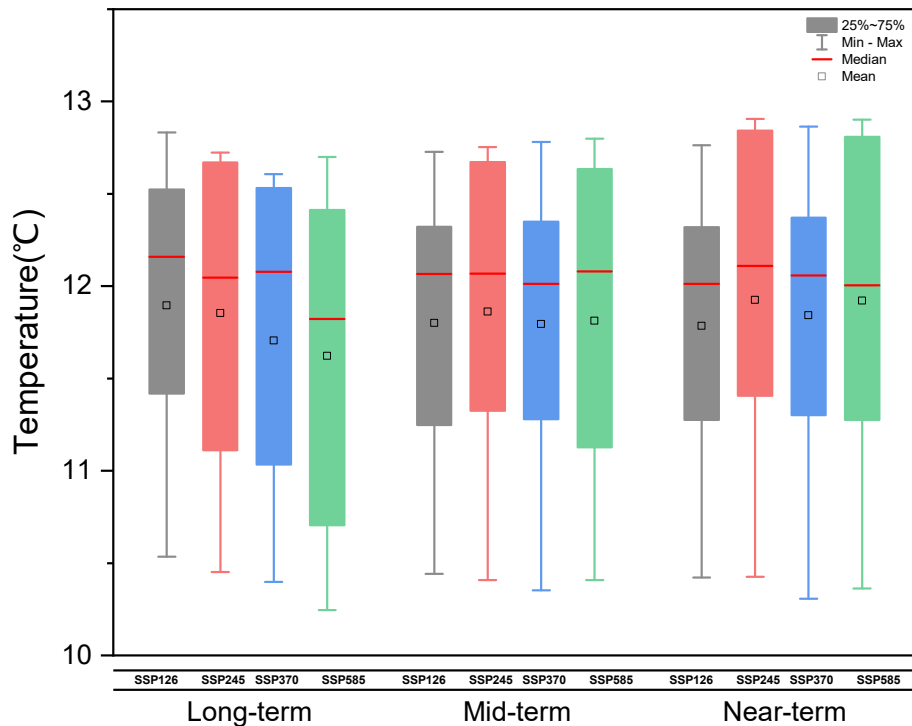
Fig. 9. Ranges of projected DTR by each selected CMIP6 model over the Tibetan Plateau for the near-term, mid-term and long-term subperiods under different SSP scenarios (units: °C). Box-and-whisker plots show the MME, median, minimum, maximum, and the 25th and 75th percentiles values of the selected CMIP6 models.

SSP5-8.5 scenarios over the 21st century is reasonably reliable.

4.   Conclusion

In this study, we assessed the simulation capabilities of 23 CMIP6 climate models regarding the spatial distribution and temporal changes of DTR climate states on the Tibetan Plateau. We compared the models with CN05.1 observational data to explore the temporal and spatial variation characteristics of DTR from 1995 to 2014. Then, we identified 11 models—BCC-CSM2-MR, EC-Earth3, EC-Earth3-CC, EC-Earth3-Veg, EC-Earth3-Veg-LR, FGOALS-g3, FIO-ESM-2-0, GFDL-ESM4, MPI-ESM1-2-HR, MPI-ESM1-2-LR, and INM-CM5-0—as those that most effectively reproduced specific spatial and temporal evolution characteristics and spatial distribution features. Ultimately, the DTR over the Tibetan Plateau under various SSP scenarios for the near, middle, and long term of future projection was then analyzed using the 11 selected models with robust performance.

The analysis revealed varying degrees of overestimation or underestimation among models in different regions of the Tibetan Plateau. Notably, EC-Earth3-CC, EC-Earth3-Veg, EC-Earth3, MPI-ESM1-2-HR, and MPI-ESM1-2-LR succeeded in replicating the spatial distribution of the climatic mean state of DTR. AWI-CM-1-1-MR, CAS-ESM22-0, BCC-CSM2-MR, EC-Earth3, EC-Earth3-CC, EC-Earth3-Veg, EC-Earth3-Veg-LR, FGOALS-g3, FIO-ESM-2-0, and

MPI-ESM1-2-HR showed good spatial correlation with observations, with correlation coefficients above 0.65. Regarding the month-to-month DTR variations from 1995 to 2014, EC-Earth3-CC, EC-Earth3-Veg, MPI-ESM1-2-HR, and MPI-ESM1-2-LR showed better alignment in reproducing the peak and trough occurrence times. However, MPI-ESM1-2-HR and MPI-ESM1-2-LR slightly underestimated peak values compared to actual observations, while EC-Earth3-CC and EC-Earth3-Veg were closer to observed values. CanESM5, CAS-ESM2-0, EC-Earth3-CC, EC-Earth3-Veg, EC-Earth3, EC-Earth3-Veg-LR, MPI-ESM1-2-HR, IPSL-CM6A-LR, MPI-ESM1-2-LR, and GFDL-ESM4 had good temporal correlation with observations, with correlation coefficients reaching above 0.9. As a result, models with a temporal correlation coefficient greater than 0.65, spatial correlation coefficient greater than 0.3, RMSE less than 0.75, and standard deviation ratio between 0.65 and 1 were identified as having relatively good simulation performance for further projection. These CMIP6 models were BCC-CSM2-MR, EC-Earth3, EC-Earth3-CC, EC-Earth3-Veg, EC-Earth3-Veg-LR, FGOALS-g3, FIO-ESM-2-0, GFDL-ESM4, MPI-ESM1-2-HR, MPI-ESM1-2-LR, and INM-CM5-0.

The selected models were then used to project the spatial distribution and temporal trends of DTR across different subperiods of the 21st century under various SSP scenarios. The results of the multimodel median of the selected CMIP6 models showed changes in DTR based on radiative forcing, with a decrease observed under higher radiative forc-

ing scenarios. Under the SSP1-2.6 scenario, a marginal rise in the annual mean value of DTR was observed on the Tibetan Plateau. However, as the radiative forcing of SSP scenarios intensifies, there are increasing trends of DTR from the near- to long-term periods. Under the SSP1-2.6, SSP2-4.5, SSP3-7.0, and SSP5-8.5 scenario, the trends of changes in DTR are 0.018°C, −0.011°C, −0.024°C, and −0.051°C $(10 \text{ yr})^{-1}$, respectively. Under the different subperiods, the changes in trends are slightly different. In the 2022–2040 subperiod, the trends in DTR on the Tibetan Plateau varies at rates of 0.023°C, −0.053°C, −0.035°C, and −0.043°C $(10 \text{ yr})^{-1}$ under the SSP1-2.6 to SSP5-8.5 scenarios, respectively, compared to the historical period of 1995–2014. In 2041–2060, the projected trends in DTR are estimated at 0.012°C, −0.033°C, −0.01°C, and −0.02°C $(10 \text{ yr})^{-1}$, respectively. Towards the end of the century (2081–2100), projected trends of 0.02°C, −0.01°C, −0.017°C, and −0.049°C $(10 \text{ yr})^{-1}$ are expected, ranked according to the radiative forcing of SSP scenarios from lowest to highest. Notably, specific regions like the southeastern edge of the Tibetan Plateau, western hinterlands of the Tibetan Plateau, southern Kunlun, and Qaidam basins exhibit more substantial changes in DTR due to factors such as altitude, topographic distinctions, and human activities.

The direct reasons behind the DTR trend changes under different SSP scenarios were analyzed. The slower warming pace of $T_{\max}$ compared to $T_{\min}$ leads to differential declining trends in DTR over the Tibetan Plateau during the mid and late 21st century. As the radiative forcing intensity of the SSP scenarios increases, this factor leads to a more pronounced decline in DTR.

The future changes in DTR in East Asia or globally also exhibit certain decreasing trends (Liu et al., 2022; Wang et al., 2024). However, in comparison to these results, the decreasing trend in DTR on the Tibetan Plateau is more pronounced than in East Asia or globally. We anticipate that this research will deepen our comprehension of the climate features related to DTR on the Tibetan Plateau, potentially assisting in addressing the potential risks linked to future DTR changes in this region. Furthermore, in future work, we will further investigate the physical mechanisms underlying the decreasing DTR under the SSP scenarios on the Tibetan Plateau.

REFERENCES

Braganza, K., D. J. Karoly, and J. M. Arblaster, 2004: Diurnal temperature range as an index of global climate change during the twentieth century. *Geophys. Res. Lett.*, **31**(13), L13217, https://doi.org/10.1029/2004GL019998.

Christidis, N., D. Mitchell, and P. A. Stott, 2019: Anthropogenic climate change and heat effects on health. *International Journal of Climatology*, **39**(12), 4751−4768, https://doi.org/10.1002/joc.6104.

Cui, T., C. Li, and F. Q. Tian, 2021: Evaluation of temperature and precipitation simulations in CMIP6 models over the Tibetan Plateau. *Earth and Space Science*, **8**(7), e2020EA001620, https://doi.org/10.1029/2020EA001620.

Di Luca, A., A. J. Pitman, and R. de Elía, 2020: Decomposing temperature extremes errors in CMIP5 and CMIP6 models. *Geophys. Res. Lett.*, **47**(14), e2020GL088031, https://doi.org/10.1029/2020GL088031.

Duan, A. M., and G. X. Wu, 2006: Change of cloud amount and the climate warming on the Tibetan Plateau. *Geophys. Res. Lett.*, **33**(22), L22704, https://doi.org/10.1029/2006GL027946.

Eyring, V., S. Bony, G. A. Meehl, C. A. Senior, B. Stevens, R. J. Stouffer, and K. E. Taylor, 2016: Overview of the Coupled Model Intercomparison Project Phase 6 (CMIP6) experimental design and organization. *Geoscientific Model Development*, **9**(5), 1937−1958, https://doi.org/10.5194/gmd-9-1937-2016.

Hamal, K., S. Sharma, R. Talchabhadel, M. Ali, Y. P. Dhital, T. L. Xu, and B. Dawadi, 2021: Trends in the Diurnal temperature range over the southern slope of Central Himalaya: Retrospective and prospective evaluation. *Atmosphere*, **12**(12), 1683, https://doi.org/10.3390/atmos12121683.

Hansen, J., M. Sato, and R. Ruedy, 1995: Long-term changes of the diurnal temperature cycle: Implications about mechanisms of global climate change. *Atmospheric Research*, **37**, 175−209, https://doi.org/10.1016/0169-8095(94)00077-Q.

Hawkins, E., and R. Sutton, 2011: The potential to narrow uncertainty in projections of regional precipitation change. *Climate Dyn.*, **37**, 407−418, https://doi.org/10.1007/s00382-010-0810-6.

Hu, Q., W. Hua, K. Q. Yang, J. Ming, P. Ma, Y. Zhao, and G. Z. Fan, 2022: An assessment of temperature simulations by CMIP6 climate models over the Tibetan Plateau and differences with CMIP5 climate models. *Theor. Appl. Climatol.*, **148**, 223−236, https://doi.org/10.1007/s00704-022-03944-6.

IPCC, 2021: *Climate Change 2021: The Physical Science Basis: Contribution of Working Group I to the sixth Assessment Report of the Intergovernmental Panel on Climate Change*. Cambridge University Press, Cambridge, United Kingdom and New York, NY, USA, https://doi.org/10.1017/9781009157896.

Karl, T. R., G. Kukla, V. N. Razuvayev, M. J. Changery, R. G. Quayle, R. R. Heim Jr., D. R. Easterling, and C. B. Fu, 1991: Global warming: Evidence for asymmetric diurnal temperature change. *Geophys. Res. Lett.*, **18**(12), 2253−2256, https://doi.org/10.1029/91GL02900.

Karl, T. R., and Coauthors, 1993: A new perspective on recent global warming: Asymmetric trends of daily maximum and minimum temperature. *Bull. Amer. Meteor. Soc.*, **74**(6), 1007−1024, https://doi.org/10.1175/1520-0477(1993)074<1007:ANPORG>2.0.CO;2.

Lewis, S. C., and D. J. Karoly, 2013: Evaluation of historical diurnal temperature range trends in CMIP5 models. *J. Climate*, **26**, 9077−9089, https://doi.org/10.1175/JCLI-D-13-00032.1.

Liu, L., Z. Z. Dong, H. N. Gong, L. Wang, W. Chen, and R. G. Wu, 2022: Climatology and trends of wintertime diurnal temperature range over East Asia in CMIP6 models: Evaluation and attribution. *Atmospheric Research*, **280**, 106438, https://doi.org/10.1016/j.atmosres.2022.106438.

Lobell, D. B., 2007: Changes in diurnal temperature range and national cereal yields. *Agricultural and Forest Meteorology*, **145**, 229−238, https://doi.org/10.1016/j.agrformet.2007.05.002.

New, M., M. Hulme, and P. Jones, 2000: Representing twentieth-century space–time climate variability. Part II: Development of 1901−96 monthly grids of terrestrial surface climate. *J. Climate*, **13**, 2217−2238, https://doi.org/10.1175/1520-0442(2000)013<2217:RTCSTC>2.0.CO;2.

Ren, G. Y., and Y. Q. Zhou, 2014: Urbanization effect on trends of extreme temperature indices of national stations over Mainland China, 1961−2008. *J. Climate*, **27**, 2340−2360, https://doi.org/10.1175/JCLI-D-13-00393.1.

Shahid, S., S. B. Harun, and A. Katimon, 2012: Changes in diurnal temperature range in Bangladesh during the time period 1961−2008. *Atmospheric Research*, **118**, 260−270, https://doi.org/10.1016/j.atmosres.2012.07.008.

Shen, X. J., B. H. Liu, G. D. Li, Z. F. Wu, Y. H. Jin, P. J. Yu, and D. W. Zhou, 2014: Spatiotemporal change of diurnal temperature range and its relationship with sunshine duration and precipitation in China. *J. Geophys. Res.: Atoms.*, **119**(23), 13 163−13 179, https://doi.org/10.1002/2014JD022326.

Stone, D., and A. Weaver, 2003: Factors contributing to diurnal temperature range trends in twentieth and twenty-first century simulations of the CCCma coupled model. *Climate Dyn.*, **20**, 435−445, https://doi.org/10.1007/s00382-002-0288-y.

Su, F. G., X. L. Duan, D. L. Chen, Z. C. Hao, and L. Cuo, 2013: Evaluation of the global climate models in the CMIP5 over the Tibetan Plateau. *J. Climate*, **26**, 3187−3208, https://doi.org/10.1175/JCLI-D-12-00321.1.

Vose, R. S., D. R. Easterling, and B. Gleason, 2005: Maximum and minimum temperature trends for the globe: An update through 2004. *Geophys. Res. Lett.*, **32**(23), L23822, https://doi.org/10.1029/2005GL024379.

Wang, F. X., C. Zhang, Y. Peng, and H. C. Zhou, 2014: Diurnal temperature range variation and its causes in a semiarid region from 1957 to 2006. *International Journal of Climatology*, **34**(2), 343−354, https://doi.org/10.1002/joc.3690.

Wang, H., and Coauthors, 2022a: Assessment and prediction of extreme temperature indices in the North China Plain by CMIP6 climate model. *Applied Sciences*, **12**(14), 7201, https://doi.org/10.3390/app12147201.

Wang, K., and G. D. Clow, 2020: The diurnal temperature range in CMIP6 models: Climatology, variability, and evolution. *J. Climate*, **33**, 8261−8279, https://doi.org/10.1175/JCLI-D-19-0897.1.

Wang, K., H. Ye, F. Chen, Y. Z. Xiong, and C. P. Wang, 2012: Urbanization effect on the diurnal temperature range: Different roles under solar dimming and brightening. *J. Climate*, **25**, 1022−1027, https://doi.org/10.1175/JCLI-D-10-05030.1.

Wang, K. C., and R. E. Dickinson, 2013: Contribution of solar radi-ation to decadal temperature variability over land. *Proceedings of the National Academy of Sciences of the United States of America*, **110**(37), 14 877−14 882, https://doi.org/10.1073/pnas.1311433110.

Wang, S. S., W. Q. Xie, and X. D. Yan, 2022b: Evalution on CMIP6 model simulation of the diurnal temperature range over China. *Climatic and Environmental Research*, **27**(1), 79−93, https://doi.org/10.3878/j.issn.1006-9585.2021.21063. (in Chinese with English abstract)

Wang, S. S., M. Zhang, J. P. Tang, X. D. Yan, C. B. Fu, and S. Y. Wang, 2024: Interannual variability of diurnal temperature range in CMIP6 projections and the connection with large-scale circulation. *Climate Dyn.*, https://doi.org/10.1007/s00382-024-07107-3.

Wild, M., and Coauthors, 2005: From dimming to brightening: Decadal changes in solar radiation at Earth's surface. *Science*, **308**(5723), 847−850, https://doi.org/10.1126/science.1103215.

Wu, G. X., Y. M. Liu, X. Liu, A. M. Duan, and X. Y. Liang, 2005: How the heating over the Tibetan Plateau affects the Asian climate in summer. *Chinese Journal of Atmospheric Sciences*, **29**(1), 47−56, https://doi.org/10.3878/j.issn.1006-9895.2005.01.06. (in Chinese with English abstract)

Wu, J., and X. J. Gao, 2013: A gridded daily observation dataset over China region and comparison with the other datasets. *Chinese Journal of Geophysics*, **56**(4), 1102−1111, https://doi.org/10.6038/cjg20130406. (in Chinese with English abstract)

Yao, T. D., and Coauthors, 2012: Different glacier status with atmospheric circulations in Tibetan Plateau and surroundings. *Nature Climate Change*, **2**, 663−667, https://doi.org/10.1038/nclimate1580.

You, Q. L., D. Wang, Z. H. Jiang, and S. C. Kang, 2017: Diurnal temperature range in CMIP5 models and observations on the Tibetan Plateau. *Quart. J. Roy. Meteor. Soc.*, **143**(705), 1978−1989, https://doi.org/10.1002/qj.3057.

You, Q. L., J. Z. Min, Y. Jiao, M. Sillanpää, and S. C. Kang, 2016: Observed trend of diurnal temperature range in the Tibetan Plateau in recent decades. *International Journal of Climatology*, **36**(6), 2633−2643, https://doi.org/10.1002/joc.4517.

Zhou, L. M., R. E. Dickinson, P. Dirmeyer, A. G. Dai, and S. K. Min, 2009b: Spatiotemporal patterns of changes in maximum and minimum temperatures in multi-model simulations. *Geophys. Res. Lett.*, **36**(2), L02702, https://doi.org/10.1029/2008GL036141.

Zhou, L. M., A. G. Dai, Y. J. Dai, R. S. Vose, C. Z. Zou, Y. H. Tian, and H. S. Chen, 2009a: Spatial dependence of diurnal temperature range trends on precipitation from 1950 to 2004. *Climate Dyn.*, **32**, 429−440, https://doi.org/10.1007/s00382-008-0387-5.

Zhu, Y. Y., and S. N. Yang, 2020: Evaluation of CMIP6 for historical temperature and precipitation over the Tibetan Plateau and its comparison with CMIP5. *Advances in Climate Change Research*, **11**(3), 239−251, https://doi.org/10.1016/j.accre.2020.08.001.